Revision #2 June 10th, 2014

High-pressure elasticity of sodium majorite garnet, $Na_2MgSi_5O_{12}$

Mainak Mookherjee[1]

[1]Earth and Atmospheric Sciences, Cornell University, Ithaca, NY 14850

[1]mainak.mookherjee@cornell.edu

Abstract

Garnet is the second most abundant mineral phase in the upper mantle and transition zone settings. The crystal structure of garnet is quite flexible and hence it is able to accommodate various cations, including large incompatible cation such as sodium. We used *first principles* simulation based on density functional theory and two widely used approximations- local density approximation (LDA) and generalized gradient approximation (GGA)- to explore the crystal structure, equation of state, and elasticity of sodium bearing majorite garnet with $Na_2MgSi_5O_{12}$ stoichiometry at pressures relevant to the upper mantle and transition zone. We find that the pressure-volume results based on LDA can be explained by a Birch Murnaghan finite strain equation of state with V_0 = 1447.6 (± 0.1) Å^3, K_0 = 177.4 (± 0.4) GPa, and K_0' = 3.93 (± 0.02). The results based on GGA can be explained by a Birch Murnaghan finite strain equation of state with V_0 = 1525.8 (± 0.2) Å^3, K_0 = 160.2 (± 0.4) GPa, and K_0' = 3.96 (± 0.02). The full elastic moduli tensor for Na-majorite with tetragonal symmetry exhibits slight deviation from the cubic symmetry with $C_{11} < C_{33}$, $C_{12} \sim C_{13}$, and $C_{44} \sim C_{66}$. The magnitude of the tetragonal strain also captures the slight deviation from the cubic symmetry. At pressures corresponding to the upper mantle and mantle transition zone, the compressional wave velocity, V_P, and shear wave velocity, V_S, for the Na-majorite garnet are fast compared to a wide variety of garnets such as pyrope, grossular, almandine, and majorite garnet. Although single crystal anisotropy

of Na-majorite is greater than pyrope, it is still low compared to the major mantle phases.

Key words: Elasticity, Equation of state, Sodium majorite, Mantle transition region

1. Introduction

In the mineralogical models of the deep Earth, garnet is a volumetrically dominant mineral phase in the upper mantle and transition zone (Ringwood, 1962). In a homogenous pyrolite model, modal abundance of garnet ranges from 20 vol % at upper mantle conditions to almost 40 vol % at transition zone conditions. The thermodynamic stability of garnet enhances upon complete dissolution of the pyroxene phase at transition zone conditions. In recent studies, it has been suggested that the Earth's mantle is far from homogenous and consists of a mixture of depleted harzburgite components and subducted oceanic crusts, or mid oceanic basalt (MORB) components (Xu et al., 2008; Stixrude and Lithgow-Bertelloni, 2012). The bulk chemistry of MORB is different from depleted harzburgite and has significantly greater proportions of incompatible elements including Na_2O (~1.5-1.8 wt%) (Irifune and Ringwood, 1993). The alkali component is likely to be incorporated into pyroxene (Angel et al., 1988) and also into garnet at higher pressures (Irifune and Ringwood, 1993). Experimental studies on realistic mantle bulk compositions have shown Na-majorite to be stable at conditions relevant to the lower part of the upper mantle and transition zone (Gasparik, 1990; Bindi et al., 2011; Bobrov et al., 2008a,b, 2009; Dymshits et al., 2010, 2013). Sodium bearing natural garnets with (Na_2O > 1 wt %) have also been reported (Sobolev and Lavrentev, 1971), indicating that sodium is likely to be an important component within the garnet structure at higher pressures.

Na-Majorite is an important host for the alkali elements and the partitioning of alkali elements might affect the relative thermodynamic stability of other alkali bearing aluminous phases such as new aluminous phases (NAL) and calcium ferrite structured (CF) phases (Dymshits et al., 2013). Owing to the importance of Na-majorite in the upper mantle and transition zone conditions, extensive studies have been conducted on phase relations (Gasparik, 1990; Bindi et al., 2011; Bobrov et al., 2008a,b, 2009; Dymshits et al., 2010, 2013), crystal structure determinations (Bindi et al., 2011) and high pressure compressibility and the equation of state (Hazen et al., 1994; Dymshits et al., 2014). It is known that the bulk sound velocity i.e., compressional wave velocity, V_P, and shear wave velocity, V_S, for mineral phases and aggregates are important to relate seismological observation with the chemical composition of the mantle. The elastic moduli for majorite garnet with $Na_2MgSi_5O_{12}$ stoichiometry are important. A complete knowledge of these end-member properties is instrumental in developing a thermodynamic mixing-model that will allow predictions for the seismic velocity for complex majorite solid solutions. It will also help us to test whether these phases that host alkali elements play important role in the upper mantle and in the transition zone. Despite being important, the full elastic moduli tensor and the sound wave velocity of $Na_2MgSi_5O_{12}$ remains unknown. In this study we used *first principles* method to predict crystal structure, equation of state, and full elastic moduli tensor at high pressures.

2. Method

2. 1. Crystal structure models for sodium garnet

In this study we examine Na-majorite garnet with $Na_2MgSi_5O_{12}$ stoichiometry. Earlier experimental studies on Na-majorite with $[(Na_{1.88}Mg_{1.12})(Mg_{0.06}Si_{1.94})Si_3O_{12}]$

stoichiometry reported a cubic symmetry with $Ia\bar{3}d$ spacegroup (Pacalo et al., 1992; Hazen et al., 1994). Recent high-pressure synthesis of Na-majorite with $Na_2MgSi_5O_{12}$ stoichiometry and subsequent crystal structure determination suggested a tetragonal symmetry with $I4_1/acd$ spacegroup (# 142) (Bindi et al., 2011). In the tetragonal Na-majorite garnet, the Na and Mg cations disordered over the two do-decahedral sites with 16e and 8b Wyckoff symmetry (Bindi et al., 2011). In our study we use the tetragonal crystal structure as our starting model. Since our calculations are static, we let the sodium cations reside in the 16e and the Mg cations reside in the 8b sites. This preserves the tetragonal symmetry with $I4_1/acd$ spacegroup (**Table 1**). The Si cations are hosted in the octahedral and tetrahedral sites. There are two crystallographically distinct tetrahedral sites (**Table 1**, **Figure 1**).

2. 2. First principle simulations

We performed first principles calculation based on the density functional theory (Kohn and Sham, 1965) (DFT) using Vienna Ab initio Simulation Package (VASP) (Kresse and Hafner, 1993; Kresse and Furthmüller, 1996a,b). Two widely used approximations to the exchange-correlation functional: the local density approximation (LDA) and generalized gradient approximation (GGA) were used (Ceperley and Adler, 1980; Perdew and Wang 1986; Perdew et al., 1991, 1996). In order to facilitate solving the DFT equations, further approximations are made motivated by the argument that the core electrons participate little in bonding and structural changes. We have employed the pseudopotential method (Heine, 1970). DFT calculations have been instrumental in accurate prediction of energetics, physical properties such as compressibility, equation of state, and elasticity of mineral phases that are relevant for the Earth and planetary interiors (Karki et al., 2001; Oganov et

al., 2002; Wentzcovitch and Stixrude, 2010;) including alkali bearing mineral phases (Mookherjee and Steinle-Neumann, 2009a,b; Mookherjee, 2011; Walker, 2012) and garnet (Li et al., 2007; Kawai and Tsuchiya, 2012; Erba et al., 2014). The pseudopotentials were successfully tested in previous studies on mineral phases and melts (Mookherjee, 2011; Mookherjee and Bezacier, 2012; Mookherjee et al., 2012).

All computations are performed in a non-primitive unit-cell with 160 atoms. We use an energy cutoff of E_{cut} = 600 eV and a K-point mesh sampling of $2\times2\times2$ *k*-point mesh. A series of convergence tests demonstrated that these computational parameters yield pressures and total energies that are converged to within 0.01 GPa and 10 meV/atom respectively. Similar computational parameters were successfully used in recent study on grossular garnet (Kawai and Tsuchiya, 2012).

We analyzed the bulk compression behavior using a third order Birch Murnaghan equation-of state (Birch, 1978). To compute the full elastic moduli tensor, we strained the lattice and let the internal degree of freedom of the crystal structure relax consistent with the symmetry: elastic moduli were obtained through the changes in stress tensor ($\underline{\underline{\sigma}}$) with respect to applied strain ($\underline{\underline{\varepsilon}}$). We applied positive and negative strain ($\underline{\underline{e}}$) of magnitude 1% in order to accurately determine stress ($\underline{\underline{\sigma}}$) in the appropriate limit of zero strain. The strained lattice ($\vec{a'}$) is related to the fully relaxed lattice ($\vec{a}$) by $\vec{a'} = (\underline{\underline{I}} + \underline{\underline{e}}) \times \vec{a}$, where $\underline{\underline{I}}$ is an identity matrix (Karki et al., 1997). The details of the method is outlined in previous studies (Karki et al., 2001). For the Na-majorite with tetragonal symmetry and $I4_1/acd$ spacegroup, four strains ($\underline{\underline{e}}$) were used to derive the six independent elastic moduli $C_{11}(=C_{22})$, C_{12}, $C_{13}(=C_{23})$, C_{33}, $C_{44}(=C_{55})$, and C_{66} (Nye, 1985).

3. Results

125 **3. 1. Equation of state and Linear Compressibility**

126 The predicted pressure-volume results based on *first-principles* simulations
127 can be explained by a Birch Murnaghan finite strain formulation (Birch, 1978),

128 $$P = 3K_0 f_V (1 + 2f_V)^{5/2}\left(1 + \frac{3}{2}(K_0' - 4)f_V\right) \quad (1)$$

129 where, f_V is Eulerian finite volume strain-

130 $$f_V = \frac{1}{2}\left(\left(\frac{V_0}{V}\right)^{2/3} - 1\right) \quad (2)$$

131 LDA predictions yields equation of state parameters with V_0 = 1447.6 (± 0.1) Å^3, K_0 =
132 177.3 (± 0.3) GPa, and K_0' = 3.93 (± 0.02). In contrast, predictions based on GGA
133 yields equation of state parameters, V_0 = 1525.8 (± 0.2) Å^3, K_0 = 160.2 (± 0.4) GPa,
134 and K_0' = 3.96 (± 0.02). The zero-pressure volume predicted using LDA and GGA are
135 1.9 % smaller and 5.4 % larger than the recent experimental results respectively
136 (Dymshits et al., 2014) (**Table 2, Figure 1**). The zero-pressure bulk modulus
137 predicted using LDA is 2% smaller than the experimental result. The discrepancy
138 between the zero-pressure bulk modulus predicted using GGA and experimental study
139 is significantly larger ~ 9.6 % (**Table 2, Figure 1**). The zero-pressure bulk modulus
140 (K_0) and volume (V_0) are anti-correlated as observed in several mineral phases
141 (Karki et al., 2001; Oganov et al., 2002). In comparison to the LDA prediction, the
142 equation of state studies on single crystal Na-majorite with
143 $[(Na_{1.88}Mg_{1.12})(Mg_{0.06}Si_{1.94})Si_3O_{12}]$ stoichiometry reports slightly stiffer ~ 7.4 %, with
144 zero-pressure bulk modulus of 191.5 (± 2.5) GPa (Hazen et al., 1994). This
145 discrepancy is likely related to the limited pressure (< 5 GPa) range explored in the
146 previous experiments. However, in an earlier Brillouin scattering study with the same
147 single crystal of Na-majorite with $[(Na_{1.88}Mg_{1.12})(Mg_{0.06}Si_{1.94})Si_3O_{12}]$ stoichiometry, a

148 zero-pressure bulk modulus of 173.5 (± 2.6) GPa (Pacalo et al., 1992) was reported.
149 This is within ~2 % of the LDA prediction (**Table 2**).

150 The pressure dependence *a*- and *c*- lattice parameters (**Supplementary Table**
151 **1**) could be explained by finite strain formulations (Meade and Jeanloz, 1990 *and*
152 *references therein*), where the Eulerian finite lattice strain, f_α, along the α i.e., *a*- and
153 *c*-axes-

154 $$f_a = \frac{1}{2}\left(\left(\frac{a_0}{a}\right)^2 - 1\right) \quad (3)$$

155 and

156 $$f_a = \frac{1}{2}\left(\left(\frac{c_0}{c}\right)^2 - 1\right) \quad (4)$$

157 and, the normalized pressure F_α, along α i.e., *a*- and *c*- axes directions are given by,

158 $$F_a = \frac{P(ac_0/a_0c)^{2/3}}{f_a(1+f_V)^{5/2}} \quad (5)$$

159 and

160 $$F_c = \frac{P(a_0c/ac_0)^{4/3}}{f_c(1+f_V)^{5/2}} \quad (6)$$

161 where f_V, is the Eulerian finite volume strain, defined in eq (2).

162 The finite strain expansions for the linear parameters (Meade and Jeanloz, 1990)
163 could be written as:

164 $$F_\alpha = K_\alpha + m_\alpha f_\alpha \quad (7)$$

165 where, K_α is the linear moduli, f_α is the finite lattice strain, m_α is related to elastic
166 constants, and α corresponds to the *a*- and *c*- axes directions. The finite strain
167 formulation using LDA yields K_a = 476 GPa and K_c = 602 GPa, whereas GGA
168 predicts softer linear moduli with K_a = 456 GPa and K_c = 539 GPa (**Figure 1**, **Table**

169 **2**). The linear moduli obtained from the finite strain fits to pressure dependence of *a*-
170 and *c*- lattice parameters are within 15% of the linear moduli predicted from the
171 experimental bulk modulus for a cubic Na-majorite i.e., $3K_0 = K_\alpha$ (~ 520.5 GPa, *l*
172 refers to linear) (Pacalo et al., 1992). The linear moduli predicted using LDA and
173 GGA methods, using the finite strain fits of *a*- and *c*- lattice parameters are consistent
174 with the zero pressure bulk modulus i.e., $K_0^{-1} = 2K_a^{-1} + K_c^{-1}$.

175 Among the polyhedral units, the dodecahedral sites have the largest zero
176 pressure volume followed by octahedral and tetrahedral sites with the relation $V_0^{NaO_8} >$
177 $V_0^{MgO_8} > V_0^{SiO_6} > V_0^{SiO_4}$, whereas, the tetrahedral sites are the stiffest followed by the
178 octahedral and the dodecahedral sites i.e., $K_0^{NaO_8} < K_0^{MgO_8} < K_0^{SiO_6} < K_0^{SiO_4}$. The
179 relationship holds for both the LDA and GGA predictions (**Table 2**).
180
181 **3. 2. Elasticity**

182 The crystal structure of Na-majorite garnet with $Na_2MgSi_5O_{12}$ stoichiometry
183 has tetragonal symmetry ($I4_1/acd$ spacegroup) and, hence, it has six independent
184 elastic moduli. We note that both LDA and GGA predictions show that the principal
185 elastic moduli along the x- and y- axes, C_{11} is softer than the principal elastic moduli
186 along the z-axes, C_{33}. The off-diagonal elastic moduli are nearly identical, i.e.,
187 $C_{12} \sim C_{13}$. The shear elastic moduli are also nearly identical, i.e., $C_{44} \sim C_{66}$. At zero-
188 pressure, the elastic moduli predicted using GGA and LDA bracket the experimental
189 full elastic moduli tensor based on Brillouin scattering on a cubic Na-majorite (Pacalo
190 et al., 1992) (**Figure 2**). The principal component, off-diagonal component, and the
191 shear elastic component of the full elastic tensor moduli stiffen upon compression

(**Figure 3**) and the pressure dependence of elastic moduli can be described by finite strain formulation (in full 4th rank tensor notation)

$$c_{ijkl} = (1+2f_V)^{7/2}[c_{ijkl0} + b_1 f_V + 0.5 b_2 f_V^2] - P\Delta_{ijkl}, \quad (8)$$

where, f_V is the Eulerian finite volume strain as defined in eq (6), and (9)

$$b_1 = 3K_0(c'_{ijkl0} + \Delta_{ijkl}) - 7c_{ijkl0}, \quad (10)$$

$$b_2 = 9K_0^2 c''_{ijkl0} + 3K'_0(b_1 + 7c_{ijkl0}) - 16b_1 - 49c_{ijkl0}, \quad (11)$$

and $\Delta_{ijkl} = -\delta_{ij}\delta_{kl} - \delta_{ik}\delta_{jl} - \delta_{il}\delta_{jk}$ (12)

where c'_{ijkl0} and c''_{ijkl0} are the first and second derivative of c_{ijkl}, with respect to pressure. Δ_{ijkl} = 1 for principal and off-diagonal elastic constants (c_{iijj} in full tensor and c_{ij} in Voigt notation, with i=1,2,3, i≠j), -1 for shear constants (c_{ijij} in full tensor notation with i=1,2,3, i≠j and c_{ij} in Voigt notation with i=4,5,6, i=j), and 0 otherwise (Karki et al. 2001). The isotropic bulk (K) and shear (G) moduli are determined using the relations

$$K_{Voigt} = (1/9)[2c_{11} + c_{33} + 2(c_{12} + 2c_{13})], \quad (13)$$

$$K_{Reuss} = [2s_{11} + s_{33} + 2(s_{12} + 2s_{13})]^{-1}, \quad (14)$$

$$G_{Voigt} = (1/15)[2c_{11} + c_{33} - (c_{12} + 2c_{13}) + 3(2c_{44} + c_{66})], \quad (15)$$

and $G_{Reuss} = 15[4(2s_{11} + s_{33} - (s_{12} + 2s_{13})) + 3(2s_{44} + s_{66})]^{-1}$ (16)

$s_{ijkl}(=c_{ijkl}^{-1})$ are the elastic compliances (inverse of the elastic constant tensor) and Voigt notation for the compliance tensor is used. Hill averages (**Table 3**) are estimated as average of Voigt and Reuss bounds.

Based on the full elastic moduli results and the resulting compliance tensors, we have determined the linear compressibility, k, which is related to the elastic compliance tensor by the relation,

$$k = s_{ij} l_i l_j \quad (17)$$

where s_{ij} is the compliance matrix in voigt notation, l_i and l_j are the directions of unit-vector (Nye 1985). For tetragonal symmetry, the linear moduli could be expressed as-

$$K_a^{-1} = k_{100} = (s_{11} + s_{12} + s_{13}) \quad (18)$$

and

$$K_c^{-1} = k_{001} = (s_{13} + s_{23} + s_{33}) \quad (19)$$

The linear moduli determined using the compliance matrix show that K_c is stiffer than K_a at low pressures, consistent with the finite strain fit to the pressure dependence of *a*- and *c*- lattice parameters (i.e., results using equation 3 to 7). The linear moduli stiffens upon compression and the relation $K_c > K_a$ is also held at higher pressures (**Figure 4**). This is similar to the relationship amongst the principal components of the full elastic moduli, i.e., $C_{33} > C_{11}$.

In our study we notice that the difference in the *a*- and *c*-lattice parameters is negligible, indicating that the deviation from cubic symmetry is rather small. We define the tetragonal strain following previous work (Heinemann et al., 1997) as difference between the *a*- and *c*-lattice parameter in the tetragonal cell with a hypothetical *a*-lattice parameter of a cubic cell with same volume, i.e.,

$$\varepsilon_{11} = \frac{a_{tet} - a_{cubic}}{a_{cubic}} \quad (20)$$

and

$$\varepsilon_{33} = \frac{c_{tet} - a_{cubic}}{a_{cubic}} \quad (21)$$

where,

$$a_{cubic} = \frac{2a_{tet} + c_{tet}}{3} \quad (22)$$

Based on the single-crystal X-ray diffraction study, at zero-pressures the tetragonal strain $\varepsilon_{11} > \varepsilon_{33}$. LDA and GGA methods predict similar results at zero pressures, however the magnitude of the ε_{11} and ε_{33} strain is smaller than the experimental values (**Figure 4**). At higher pressures, the relation between the tetragonal strains reverses with $\varepsilon_{33} > \varepsilon_{11}$ (**Figure 4**). This is likely a manifestation of the relation $K_c > K_a$ that, makes *c*- lattice parameter slightly larger than the *a*-lattice parameter at higher pressures.

The bulk compressional wave (V_P) and the shear wave (V_S) velocities obtained from the aggregate bulk and shear modulus (i.e., equation 16 to 19) increase upon compression (**Figure 5**). We computed the single crystal azimuthal anisotropy for P- (AV_P) and S- waves (AV_S) using the formulation for maximum polarization anisotropy (Mainprice, 1990)-

$$AV_P(\%) = \frac{V_{P\max} - V_{P\min}}{(V_{P\max} + V_{P\min})} \times 200 \quad (23)$$

and

$$AV_S(\%) = \frac{V_{S\max} - V_{S\min}}{(V_{S\max} + V_{S\min})} \times 200 \quad (24)$$

Based on the LDA predictions, the AV_P anisotropy of Na-majorite is ~ 6.5% at low pressures and reduces to 5 % at transition zone conditions. The AV_P anisotropy is 5.1 % at low pressures and increases slightly to 5.6 % at transition zone conditions (**Figure 5**).

4. Discussion

Our *first principles* simulations indicate that the compressional wave velocity, V_P, and shear wave velocity, V_S, for Na-majorite are in good agreement with the ambient condition Brillouin scattering results (Pacalo et al., 1992). In comparison with the other garnets relevant for the upper mantle and the transition zone regions, such as, pyrope ($Mg_3Al_2Si_3O_{12}$), grossular ($Ca_3Al_2Si_3O_{12}$), almandine ($Fe_3Al_2Si_3O_{12}$), and majorite ($Mg_4Si_4O_{12}$), Na-majorite is relatively faster (**Figure 5**). The variation in the velocity of various garnet could be rationalized in terms of the specific site chemistry. For example, andradrite is iron-rich which leads to enhanced density and lower sound wave velocity, whereas in the $Na_2MgSi_5O_{12}$ garnet, the faster V_P and V_S velocities are likely to be related with stiffer bulk and shear modulus which in turn is due to the substitution of the large sodium cations into the dodecahedral site in addition to the silicon cations in the octahedral sites. A positive correlation between the large sodium cations in the dodecahedral sites and stiffer bulk and shear moduli might seem counter intuitive since among all the polyhedral units, the zero-pressure bulk modulus of the NaO_8 polyhedral unit, $K_0^{NaO_8}$ is the smallest (**Table 2**). However, the bulk and shear moduli of garnet crystal structures are controlled by the corner linked octahedral and tetrahedral units. There is a strong influence of chemistry i.e., cation size and charge in these polyhedral units on the bulk and shear modulus of garnet structure. Unlike pyrope and grossular, the octahedral units in Na-majorite are occupied by silicon cation (Si^{4+}) which has a smaller size and higher charge compared to the aluminum cation (Al^{3+}). This leads to smaller unit-cell volume of Na-majorite. In addition, the NaO_8 dodecahedral units have large proportion of shared edges and hence act as braces controlling the amount of rotation between the corner linked tetrahedral (SiO_4) and the octahedral (SiO_6) units. Since Na is a large cation, the rotational freedom within the corner linked octahedral and tetrahedral units are

minimized. This is also true for grossular that also has large Ca cations residing in the dodecahedral sites. In comparison, pyrope, with the smaller Mg cations, allows for a greater degree of freedom for the corner sharing octahedral and tetrahedral units, resulting in softer bulk and shear modulus (Pacalo et al., 1992).

In our static calculations, we have ordered the Na and Mg cations in the 16e and 8b Wyckoff symmetry. This results in a continuous edge sharing chain of NaO_8 units parallel to the 4_1 screw axes i.e., parallel to [001] direction. And hence the degree of rotational freedom for corner sharing octahedral and tetrahedral units along the 4_1 screw axes (|| [001] direction) is lower than the [100] direction. In contrast, NaO_8 units do not have continuous edge sharing along [100] and [010] directions (Figure S1). This is likely explanation for the relation $C_{33} > C_{11}$ and $K_c > K_a$ in our study.

5. Implications

Na-majorite garnet with $Na_2MgSi_5O_{12}$ stoichiometry is likely to be an important component in the deeply subducted oceanic crustal materials (Dymshits et al., 2013). The velocity of this phase is likely to be faster compared to the majorite garnet with $MgSiO_3$ stoichiometry. Na-majorite garnet with the $NaAlSi_2O_6$ stoichiometry, i.e., jadeitic pyroxene, has also been proposed to have higher bulk and shear modulus (Duffy and Anderson, 1989). However, such end member majorite garnet composition ($NaAlSi_2O_6$) has not been examined or observed in experimental studies, and the physical properties have only been estimated (Bass and Anderson, 1984). The effect of temperature on the sound velocities for the $Na_2MgSi_5O_{12}$ majorite garnet is unknown and needs to be investigated. However, recent thermal equation-of-state results indicate that the temperature derivative of the bulk modulus

309 $(\partial K_0 / \partial T)$ for $Na_2MgSi_5O_{12}$ majorite garnet (-0.0023 GPa K^{-1}) (Dymshits et al.,
310 2014) is similar to the $MgSiO_3$ majorite garnet (-0.0022 GPa K^{-1}) (Nishihara et al.,
311 2005). If the temperature derivative of the shear modulus for $Na_2MgSi_5O_{12}$ is similar
312 to $MgSiO_3$ majorite garnet (Irifune et al., 2008), then it is likely that Na- majorite
313 might still remain faster compared to majorite in the transition zone region. However,
314 reduction of velocity is required to explain the seismologicaly observed velocity
315 profiles (Dziewonski and Anderson, 1981) in the mantle and transition zone region.
316 The velocity reduction could occur through an admixture of Na-majorite and other
317 alkali bearing aluminous phases such as NAL and CF phases with slower velocity
318 (Mookherjee et al., 2012).

319 Anisotropy in velocity based on the single crystal elastic constants indicate
320 that $Na_2MgSi_5O_{12}$ has slightly larger AV_P compared to pyrope (Lu et al., 2013) but
321 lower than grossular (Kawai and Tsuchiya, 2012). Since the Na-majorite phase is not
322 very anisotropic, velocity reduction through anisotropy could be ruled out. Important
323 mantle phases such as olivine, wadsleyite, pyroxene, and calcium perovskite are
324 likely to dominate the seismic anisotropy signatures in the upper mantle and transition
325 zone region (Stixrude, 2007). Other possible mechanisms that might account for
326 reductions of seismic velocity might include incorporation of protons in the garnet
327 structure as reported in experimental studies on pyrope-rich garnet at mantle
328 conditions (Lu and Keppler, 1997; Mookherjee and Karato, 2010). Proton
329 substitutions might lead to further reduction of velocities, as has been observed for the
330 grossular garnet (O'Neill et al., 1993). However, further investigation on the effect of
331 chemistry (e.g., sodium, proton, iron) and temperature on the elasticity of majorite
332 garnet is required at conditions relevant to the lower part of the upper mantle and

transition zone region to explain the geophysical observations and to understand the composition and heterogeneity in the Earth's mantle.

Acknowledgements

MM acknowledges constructive comments from three anonymous reviewers that improved the clarity of the article. MM also acknowledges comments from Dr. Lucsa Bindi. MM is currently supported by the US National Science Foundation grant (EAR-1250477). MM acknowledges computing resources (request # EAR130015) from the Extreme Science and Engineering Discovery Environment (XSEDE), which is supported by National Science Foundation grant number OCI-1053575.

References

Angel. R. J., Gasparik, T., Ross, N. L., Finger, L. W., Prewitt, C. T., and Hazen, R. M. (1988) A silica-rich sodium pyroxene phase with six-coordinated silicon, Nature, 335, 156-158.

Bass, J. D., and Anderson, D. L. (1984) Composition of the upper mantle: Geophysical tests of two petrological model, Geophysical Research Letters, 11, 237-240.

Bindi, L., Dymshits, A. M., Bobrov, A. V., Litasov, K. D., Shatskiy, A. F., Ohtani, E., and Litvin, Y. A. (2011) Crystal chemistry of sodium in the Earth's interior: The structure of $Na_2MgSi_5O_{12}$ synthesized at 17.5 GPa and 1700 ^oC, American Mineralogist, 96, 447-450.

Birch, F. (1978) Finite strain isotherm and velocities for single crystal and polycrystalline NaCl at high-pressures and 300 K, Journal of Geophysical Research, 83, 1257-1268.

Bobrov, A. V., Kojitani, H., Akaogi, M., and Litvin, Y. A. (2008a) Phase relations on the diopside-jadeite-hedenbergite join up to 24 GPa and stability of Na-bearing majoritic garnet, Geochimica Cosmochima Acta, 72, 2392-2408.

Bobrov, A. V., Litvin, Y. A., Bindi, L., and Dymshits, A. M. (2008b) Phase relatons of sodium-rich majoritic garnet in the system $Mg_3Al_2Si_3O_{12}$-$Na_2MgSi_5O_{12}$ at 7.0 and 8.5 GPa, Contribution to Mineralogy and Petrology, 156, 243-257.

Bobrov A. V., Dymshits A. M., and Litvin Y. A. (2009) Conditions of magmatic crystallization of Na-bearing majoritic garnets in the earth mantle: evidence from experimental and natural data, Geochemical International, 10, 1011−1026.

Ceperley, D. M., and Adler, B. J. (1980) Ground state of the electron gas by a stochastic method, Physical Review Letters, 45, 566-569.

Duffy, T. S., and Anderson, D. L. (1989) Seismic velocities in mantle minerals and mineralogy of the upper mantle, Journal of Geophysical Research., 94, 1895-1912.

Dymshits A. M., Bobrov A. V., Litasov K. D., Shatskiy A. F., Ohtani, E., Litvin Y. A. (2010) Experimental study of the Pyroxene-Garnet phase transitioin in the $Na_2MgSi_5O_{12}$ system at pressure 13–20 GPa: first synthesis of sodium majorite, Dokaldy Earth Sciences, 434, 378–381.

Dymshits, A. M., Bobrov, A. V., Bindi, L., Litvin, Y. A., Litasov, K. D., Shatskiy, A. F., and Ohtani, E. (2013) Na-bearing majoritic garnet in the $Na_2MgSi_5O_{12}$-$Mg_3Al_2Si_3O_{12}$ join at 11-20 GPa: Phase relations, structural peculiarities and solid solutions, Geochimica Cosmochima Acta, 105, 1-13.

Dymshits, A. M., Litasov, K. D., Shatskiy, A., Sharygin, I. S., Ohtani, E., Suzuki, A., Pokhilenko, N. P., and Funakoshi, K. (2014) P-V-T equation of state of Na-majorite to 21 GPa and 1673 K, Physics of the Earth and Planetary Interiors,

227, 68-75.

Dziewonski, A. M., and Anderson, D. L. (1981) Preliminary reference Earth model, Physics of the Earth and Planetary Interiors, 25, 297-356.

Erba, A., Mahmoud, A., Orlando, R., and Dovesi, R. (2014) Elastic properties of six garnet end members from accurate ab initio simulations, Physics and Chemistry of Minerals, 41, 151-160.

Gasparik, T. (1990) Phase relations in the transition zone, Journal of Geophysical Research, 95, 15751-15769.

Hazen, R. M., Downs, R. T., Conrad, P. G., Finger, L. W., and Gasparik, T. (1994) Comparative compressibilities of majorite-type garnets, Physics and Chemistry of Minerals, 21, 344-349.

Heine, V. (1970) The pseudopotential concept, Solid State Physics, 24, 1-37.

Heinemann, S., Sharp, T. G., Seifert, F., and Rubie, D. C. (1997) The cubic-tetragonal phase transition in the system majorite ($Mg_4Si_4O_{12}$)- pyrope ($Mg_3Al_2Si_3O_{12}$) and garnet symmetry in the Earth's transition zone, Physics and Chemistry of Minerals, 24, 206-221.

Irifune, T., and Ringwood, A. E. (1993) Phase transformations in subducted oceanic crust and buoyancy relationships at depths of 600-800 km in the mantle, Earth and Planetary Science Letters, 117, 101-110.

Irifune, T., Higo, Y., Inoue, T., Kono, Y., Ohfuji, H., and Funakoshi, K. (2008) Sound velocities of majorite garnet and composition of the mantle transition region, Nature, 451, 814-817.

Jiang, F., Speziale, S., and Duffy, T. S. (2004) Single-crystal elasticity of grossular- and alamandine-rich garnets to 11 GPa by Brillouin scattering, Journal of Geophysical Research, 109, B10210, 1-10.

Karki, B. B., Stixrude, L., Clark, S. J., Warren, M. C., Ackland, G. J., and Crain, J. (1997), Structure and elasticity of MgO at high pressure, American Mineralogist, 82, 51-60.

Karki, B. B., Stixrude, L., and Wentzcovitch, R. M. (2001) High-pressure elastic properties of major materials of Earth's mantle from first principles, Reviews of Geophysics, 39, 507-534.

Kawai, K., and Tsuchiya, T. (2012) First principles investigations on the elasticity of grossular garnet, Journal of Geophysical Research, 117, B02202.

Kohn, W., and Sham, L. J. (1965) Self-consistent equations including exchange and correlation effects, Physical Review, 140, A1133-A1138.

Kresse, G., and Furthmüller, J. (1996a) Efficiency of ab-initio total energy calculations for metals and semiconductors, Computational Material Sciences., 6, 15-50.

Kresse, G., and Furthmüller, J. (1996b) Efficient iterative schemes for ab initio total-energy calculations using plane-wave basis set, Physical Review B 54, 11169-11186.

Kresse, G., and Hafner, J. (1993) Ab initio Molecular-Dynamics for Liquid-Metals, Physical Review B 47, 558-561.

Li, L., Weidner, D. J., Brodholt, J., and Price, G. D. (2007) The effect of cation-ordering on the elastic properties of majorite: An ab inito study, Earth and Planetary Science Letters, 256, 28-35.

Lu, C., Mao, Z., Lin, J.-F., Zhuralev, K., Tkachev, S. N., and Prakapenka, V. B. (2013) Elasticity of single-crystal iron-bearing pyrope up to 20 GPa and 750 K, Earth and Planetary Science Letters, 361, 134-142.

Lu, R., and Keppler, H. (1997) Water solubility in pyrope to 100 kbar, Contribution to

433 Mineralogy and Petrology, 129, 35-42.
434 Mainprice, D. (1990) An efficient FORTRAN program to calculate seismic
435 anisotropy from the lattice preferred orientation of minerals,
436 Computational Gesoscience, 16, 385-393.
437 Meade, C., and Jeanloz, R. (1990) Static compression of $Ca(OH)_2$ at room
438 temperature: Observations of amorphization and equation of state measurements
439 to 10.7 GPa, Geophysical Research Letters, 17, 1157-1160.
440 Mookherjee, M., and Steinle-Neumann, G. (2009a) Elasticity of phase-X at high
441 pressure, Geophysical Research Letters, 36, L08307.
442 Mookherjee, M., and Steinle-Neumann, G. (2009b) Detecting deeply subducted crust
443 from the elasticity of hollandite, Earth and Planetary Science Letters, 288, 349-
444 358.
445 Mookherjee, M., and Karato, S.-i. (2010) Solubility of water in pyrope-rich garnet at
446 high pressures and temperature, Geophysical Research Letters, 37, L03310,
447 doi:10.1029/2009GL041289.
448 Mookherjee, M. (2011) Mid-mantle anisotropy: Elasticity of aluminous phases in
449 subducted MORB, Geophysical Research Letters, 38, L14302,
450 10.1029/2011GL047923.
451 Mookherjee, M., and Bezacier, L. (2012) The low velocity layer in subduction zone:
452 Structure and elasticity of glaucophane at high pressures, Physics of Earth and
453 planetary Interiors, 208-209, 50-58.
454 Mookherjee, M., Karki, B. B., Stixude, L., and Lithgow-Bertelloni, C. (2012)
455 Energetics, equation of state, and elasticity of NAL phase: potential host for
456 alkali and aluminum in the lower mantle, Geophysical Research Letters, 39,
457 L19306, doi: 10.1029/2012GL053682.

458 Nishihara, Y., Aoki, I., Takahashi, E., Matsukage, K. N., and Funakoshi, K. (2005)
459 Thermal equation of state of majorite with MORB composition, Physics of
460 the Earth and Planetary Interiors, 148, 73-84.
461 Nye, J. F. (1957) Physical properties of crystals: Their representation by tensors and
462 matrices, Oxford Univ. Press, 329.
463 Oganov, A. R., Brodholt, J. P., and Price, G. D. (2002) Ab initio theory of
464 thermoelasticity and phase transition in minerals, European Mineralogical
465 Union notes in Mineralogy, 4, 83-170.
466 O'Neill, B., Bass, J. D., and Rossman, G. R. (1993) Elastic properties of
467 hydrogrossular garnet and implications of water in the upper mantle, Journal
468 of Geophysical Research, 98, 20,031-20,037.
469 Pacalo, R. E. G., Weidner, D. J., and Gasparik, T. (1992) Elastic properties of
470 sodium-rich majorite garnet, Geophysical Research Letters, 19, 1895-1898.
471 Perdew, J. P., Wang, Y. (1986) Accurate and simple density functional for the
472 electronic exchange energy: Generalized gradient approximation, Physical
473 Review B, 33, 8800-8802.
474 Perdew, J. P., Chevary, J. A., Vosko, S. H., Jackson, K. A., Pederson, M. R., Singh,
475 D. J., Fiolhais, C. (1991) Atoms, molecules, solids, and surfaces: Applications
476 of the generalized gradient approximation for exchange and correlation,
477 Physical Review B, 46, 6671-6687.
478 Perdew, J. P., Burke, K., Erzerhof, M. (1996) Generalized gradient approximation
479 made simple, Physical Review Letters, 77, 3865-3868.
480 Ringwood, A. E. (1962) A model for the upper mantle, Journal of Geophysical
481 Research, 67, 857-867.
482 Sinogeikin, S. V., and Bass, J. D. (2000) Single-crystal elasticity of pyrope and MgO

to 20 GPa by Brillouin scattering in the diamond cell, Physics of the Earth and Planetary Interiors, 120, 43-62.

Sobolev, N. V., and Lavrentev, Y. G. (1971) Isomorphic sodium admixture in garnets formed at high pressures, Contribution to Mineralogy and Petrolology, 31, 1-12.

Stixrude, L. (2007) Properties of rocks and minerals- Seismic properties of rocks and minerals, and the structure of the Earth, in Treatise on Geophysics, 2, Mineral Physics, edited by Shubert, G., Oxford, 7-32.

Stixrude, L., and Lithgow-Bertelloni, C. (2012) Geophysics of chemical heterogeneity in the mantle, Annual review of the Earth and Planetary Sciences, 40, 569-595.

Walker, A. M. (2012) The effect of pressure on the elastic properties and seismic anisotropy of diopside and jadeite from atomic scale simulation, Physics of the Earth and Planetary Interiors, 192-193, 81-89.

Wentzcovitch, R. M., and Stixrude, L. (2010) Theoretical and computational methods in mineral physics: Geophysical applications, Reviews of Mineralogy and Geochemistry, 71, 484.

Xu, W., Lithgow-Bertelloni, C., Stixrude, L., and Ritsema, J. (2008) The effect of bulk composition and temperature on mantle seismic structure, Earth and Planetary Science Letters, 275, 70-79.

Figure Caption

Figure 1. (***a***) Crystal structure of $Na_2MgSi_5O_{12}$ viewed down the c-axis. The eight fold coordinated Na cations (green symbols) occupy the 16e Wyckoff sites and the Mg cations (yellow symbols) occupy the 8b Wyckoff sites. Also shown are the corner-sharing octahedral units, i.e., 16c Wyckoff sites and tetrahedral units 16e and 8a Wyckoff sites (**Table 1**). Both the octahedral and tetrahedral units are fully occupied by the silicon cations represented by blue symbols. (***b***) Plot of pressure vs. volume, the filled red symbols (LDA) and blue symbols (GGA) are from this study, grey filled symbols are from experimental study (Dymshits et al., 2014). The red and blue line represents finite strain fits to LDA and GGA results. The dashed line represents the finite strain fit to the experimental results (Dymshits et al., 2014), the black filled circles represent single crystal X-ray diffraction results (Hazen et al., 1994). The inset shows the plot of Eulerian linear finite strain vs. normalized pressure along *a*- and *c*- axes. Red and blue symbols represent LDA and GGA results respectively. The error bars are calculated based on a an assumed numerical precision in the pressure of ± 0.1 GPa, (***c***) Discrepancy between the equation of state parameters from experimental studies and the results from *first principles*- Red and blue bars represents the discrepancy between the experimental results with the prediction based on LDA and GGA methods respectively. The zero-pressure volume (V_0) and bulk modulus (K_0) from LDA and GGA are compared with recent synchrotron based powder X-ray diffractions (Dymshits et al., 2014). The zero-pressure lattice parameters, i.e., a_0 and c_0 from LDA and GGA are compared with the single-crystal X-ray diffraction results (Bindi et al., 2011). The linear moduli along the *a*- and *c*- axes, i.e., K_a and K_c are compared with the linear

527 moduli determined form the bulk modulus of the cubic Na-majorite (Pacalo et
528 al., 1992).

529 **Figure 2.** The zero pressure full elastic tensor moduli (C_{ij}) for $Na_2MgSi_5O_{12}$- a
530 comparison between from Brillouin scattering study (Pacalo et al., 1992) and the
531 results from *first principles* are shown. The red, blue, and grey symbols
532 represent LDA, GGA, and the experimental results (Pacalo et al., 1992)
533 respectively. At the bottom of the figure, the red and the blue bars indicate the
534 discrepancy between the experimental results (Pacalo et al., 1992) and the
535 prediction based on LDA and GGA methods, respectively.

536 **Figure 3.** Pressure dependence of the full elastic tensor moduli (C_{ij}) for $Na_2MgSi_5O_{12}$
537 - (***a***) principal components, (***b***) off-diagonal components, (***c***) shear components,
538 and (***d***) bulk and shear moduli. Note- Red and blue symbols represents the
539 predictions based on LDA and GGA methods respectively. The solid and dashed
540 lines are finite strain fits to LDA and GGA predictions respectively. The grey
541 symbols represents Brillouin scattering results at ambient conditions (Pacalo et
542 al., 1992). The light green shaded region depicts the mantle transition zone
543 region where Na-majorite is likely to be stable.

544 **Figure 4.** Plot of linear moduli, K_a and K_c, derived from the full elastic constant
545 tensor moduli C_{ij}, as a function of pressure. The results are consistent with the
546 linear moduli at zero pressure derived from the finite strain fits to the pressure
547 dependence of *a*- and *c*-lattice parameters (**Figure 1, Table 2**). The red and blue
548 symbols refer to predictions based on LDA and GGA methods. The lines refer
549 to linear fits. The inset shows tetragonal strain, ε_{11} and ε_{33} for the single crystal
550 X-ray diffraction results (grey bars) (Bindi et al., 2011), LDA (red bars), and

GGA (blue bars) predictions. The symbols for ε_{11} are in darker shades whereas the symbols for ε_{33} are lighter in shades. At zero pressure, $a_0 > c_0$ and $\varepsilon_{11} > \varepsilon_{33}$ for the experiments, LDA, and GGA predictions. However, at higher pressure both LDA and GGA predicts a stiffer K_c and hence at high-pressures the magnitude of the strains are reversed with $\varepsilon_{33} > \varepsilon_{11}$.

Figure 5*a*. Plot of V_P and V_S as a function of pressure for garnet with varying compositions- 'py' refers to pyrope (Sinogeikin and Bass, 2000); 'gr' refers to grossular rich garnet (Jiang et al., 2004); 'and' refers to andradite rich garnet (Jiang et al., 2004); 'maj' refers to majorite (Irifune et al., 2008); 'na-maj' refers to sodium bearing majorite (Pacalo et al., 1992), and the blue and red symbols refer to the LDA and GGA results on Na-majorite with $Na_2MgSi_5O_{12}$ stoichiometry from this study. (***b***) Plot of seismic anisotropy based on single crystal elastic constant tensor for Na-majorite: AV_P (circles) and AV_S (rhombs) as a function of pressure. The red and blue symbols refer to LDA and GGA results respectively. The light green shaded region depicts the mantle transition zone region where Na-majorite is likely to be stable. Also, indicated is the thermodynamic stability range for garnets with varying chemistry.

Table 1. Fully relaxed crystal structure with Wyckoff positions, site symmetry, and fractional coordinates of atoms of $Na_2MgSi_5O_{12}$ from LDA, for a unit-cell volume of 1480 $Å^3$ (a= 11.409, and c= 11.368 Å).

Symmetry	Site Symmetry	Wyckoff Symbol	Elements	*fractional corrdinates*		
				x	*y*	*z*
			$Na_2MgSi_5O_{12}$			
$I4_1/acd$	2	16e	Na	0.1263	0.0000	0.2500
4/mmm	222	8b	Mg	0.0000	0.2500	0.1250
142	-1	16c	Si^{VI}	0.0000	0.0000	0.0000
	2	16e	Si^{IV}	0.3740	0.0000	0.2500
	-4	8a	Si^{IV}	0.0000	0.2500	0.3750
	1	32g	O	0.0360	0.0442	0.6463
	1	32g	O	0.6454	0.0375	0.0430
	1	32g	O	0.0406	0.6504	0.0294

Table 2. Equation of state parameters, linear compressibilities, and compressibilities of the polyhedral units.

	V_0 Å^3	K_0 GPa	K_0'	Reference
	1447.6(0.1)	177.3(0.3)	3.93(0.02)	LDA
	1525.8(0.2)	160.2(0.4)	3.96(0.02)	GGA
	1476.0(0.1)	181.0(0.9)	4.40(1.20)	SXRD[a]
	1484.9(0.3)	173.5(2.6)	*	SCBS[b]
	1485.5(0.3)	191.5(2.5)	4.00(*fixed*)	SCXRD[c]
	a_0 Å	K_a GPa		Reference
	11.326(0.0002)	476.4(2.9)		LDA
	11.529(0.0001)	455.6(1.9)		GGA
	11.409(0.001)	520.5(7.8)		SCBS[b]
	c_0 Å	K_c GPa		Reference
	11.284(0.0005)	601.9(2.8)		LDA
	11.479(0.0006)	539.3(2.3)		GGA
	11.409(0.001)	520.5(7.8)		SCBS[b]
	Compressibility of polyhedral units			
	V_0 Å^3	K_0 GPa	K_0'	Reference
SiO_4 (16e)	2.193(0.000)	314.9(2.1)	4.27(0.11)	LDA
	2.238(0.002)	287.1(6.7)	5.16(0.31)	GGA
SiO_4 (8a)	2.156(0.000)	318.3(3.1)	4.86(0.17)	LDA
	2.279(0.001)	281.8(3.0)	4.64(0.13)	GGA
SiO_6	7.535(0.000)	247.8(0.6)	5.27(0.04)	LDA
	7.919(0.003)	212.9(2.0)	5.37(0.10)	GGA
MgO_8	19.513(0.004)	126.0(0.5)	3.45(0.02)	LDA
	20.791(0.022)	114.7(1.7)	3.45(0.06)	GGA
NaO_8	21.232(0.005)	123.1(0.5)	3.21(0.02)	LDA
	22.609(0.012)	111.5(0.8)	3.29(0.03)	GGA

[a]synchroton X-ray diffraction (Dymshits et al., 2014); [b]single-crystal full elastic moduli tensor using Brillouin scattering (Pacalo et al., 1992) *this study was conducted at ambient conditions and hence no pressure derivatives were reported; [c]single-crystal X-ray diffraction (Hazen et al., 1994); LDA- local density approximation, *this study*; GGA- generalized gradient approximation, *this study*

Table 3. Elasticity of garnet as a function of pressure and finite strain fit with the pressure derivatives (dC_{ij}/dP) shown in brackets.

V ($Å^3$)	ρ (gm/cm^3)	P	C_{11}	C_{33}	C_{12}	C_{13}	C_{44}	C_{66}	K_{VRH}	G_{VRH}	V_P	V_S
						(GPa)					(km/sec)	
$Na_2MgSi_5O_{12}$ ($I4_1/acd$) (LDA)												
1480	3.61	-3.8	296.2	344.4	87.7	89.7	106.0	107.6	163.0	108.4	9.2	5.5
1440	3.72	0.9	323.9	368.0	102.6	101.4	109.2	110.3	180.5	112.9	9.4	5.5
1400	3.82	6.3	354.2	396.9	119.2	117.0	114.9	115.9	201.1	119.1	9.7	5.6
1360	3.93	12.5	386.5	428.8	139.0	135.0	120.8	122.1	224.2	125.4	10.0	5.6
1320	4.05	19.6	421.3	462.1	161.6	155.9	125.9	128.6	250.0	131.3	10.2	5.7
1280	4.18	27.8	459.1	497.9	188.8	181.7	133.0	134.6	279.9	137.5	10.5	5.7
1240	4.31	37.2	498.3	535.2	217.2	209.8	138.6	138.4	311.6	142.6	10.8	5.7
1200	4.46	48.1	542.3	578.6	250.1	242.6	146.3	149.3	348.1	150.1	11.1	5.8
						finite strain fit						
1448	3.70	0.0	318.5	364.1	99.6	98.6	109.6	111.0	177.0	112.1	9.4	5.5
			(5.8)	(5.5)	(3.2)	(2.9)	(0.9)	(1.0)	(3.9)	(1.2)		
$Na_2MgSi_5O_{12}$ ($I4_1/acd$) (GGA)												
1560	3.43	-3.4	254.8	309.1	71.8	79.4	95.0	95.0	141.5	96.0	8.9	5.3
1520	3.52	0.6	294.7	340.0	93.5	96.0	101.9	103.8	166.3	104.3	9.3	5.4
1480	3.61	5.2	317.4	363.0	102.8	106.0	107.7	110.4	180.5	110.6	9.5	5.5
1440	3.72	10.4	345.4	386.8	118.2	115.9	111.7	113.6	197.3	115.7	9.7	5.6
1400	3.82	16.3	378.1	415.3	137.6	132.7	119.2	121.3	219.6	123.0	10.0	5.7
1360	3.93	23.1	419.8	456.0	164.9	158.3	132.1	130.5	250.9	133.2	10.4	5.8
1320	4.05	30.9	450.9	491.9	186.9	179.8	131.9	132.4	276.1	135.5	10.6	5.8
1280	4.18	39.9	485.0	521.6	210.7	204.1	139.5	134.6	303.2	140.8	10.8	5.8
						finite strain fit						
1526	3.51	0	282.2	331.4	84.3	90.1	100.9	100.8	159.4	103.5	9.2	5.4
			(7.1)	(6.4)	(3.6)	(3.1)	(1.3)	(1.6)	(3.9)	(1.3)		

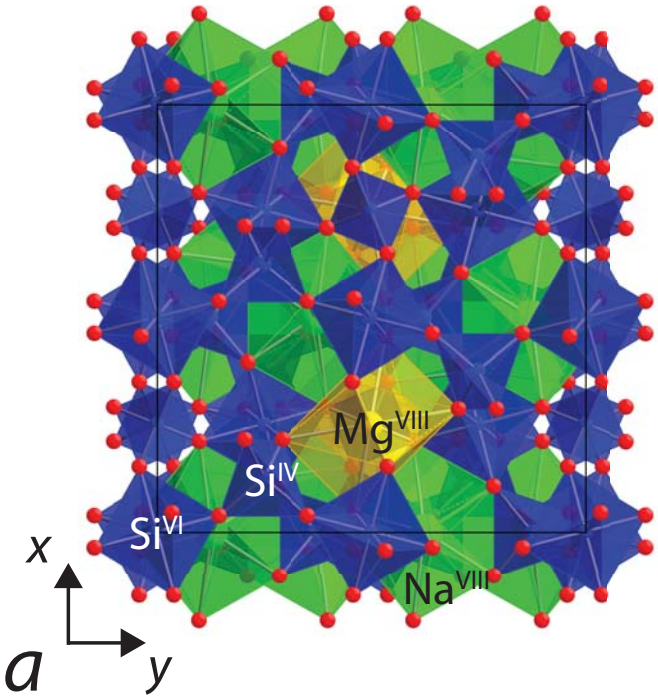
Mg^VIII
Si^IV
Si^VI
Na^VIII
x
y
a

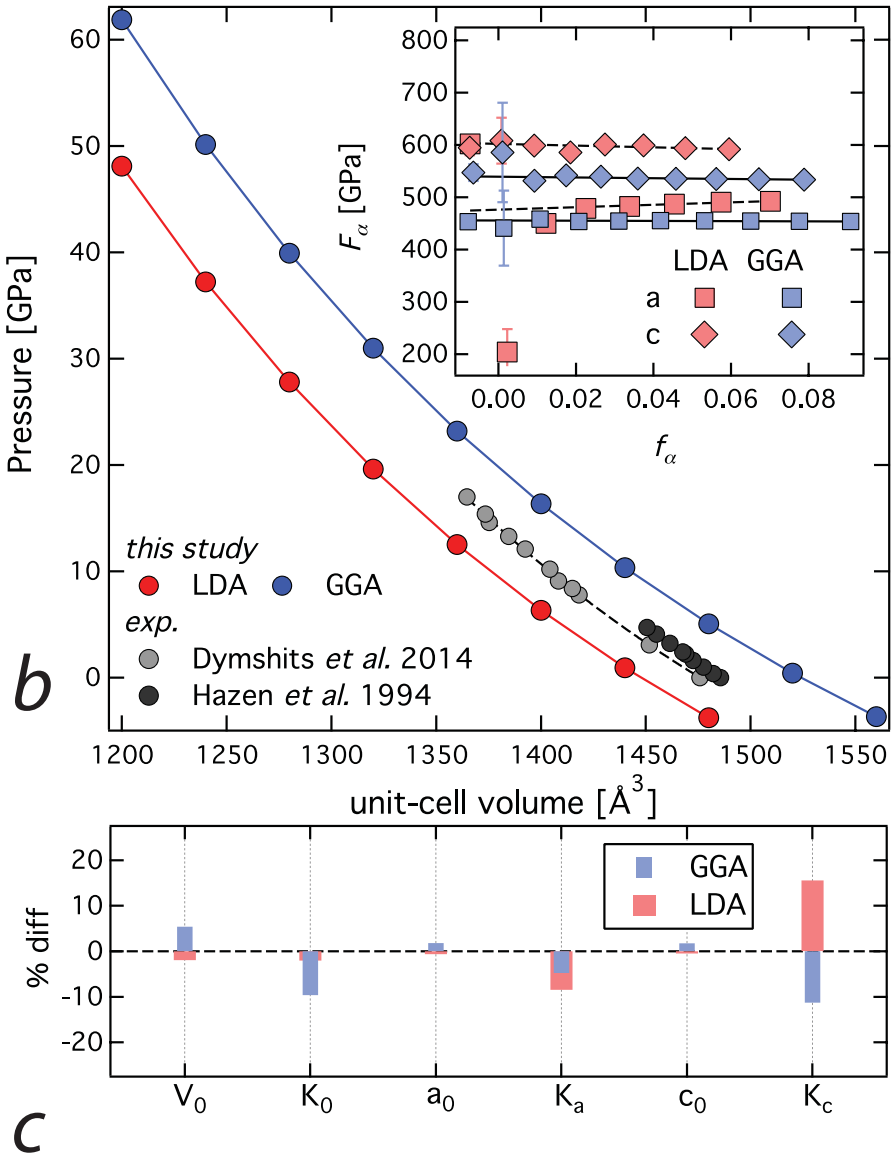
Pressure [GPa]
unit-cell volume [Å^3]
this study
LDA
GGA
exp.
Dymshits et al. 2014
Hazen et al. 1994
F_α [GPa]
f_α
LDA GGA
a
c
b
% diff
GGA
LDA
V0
K0
a0
Ka
c0
Kc
c

Figure 1

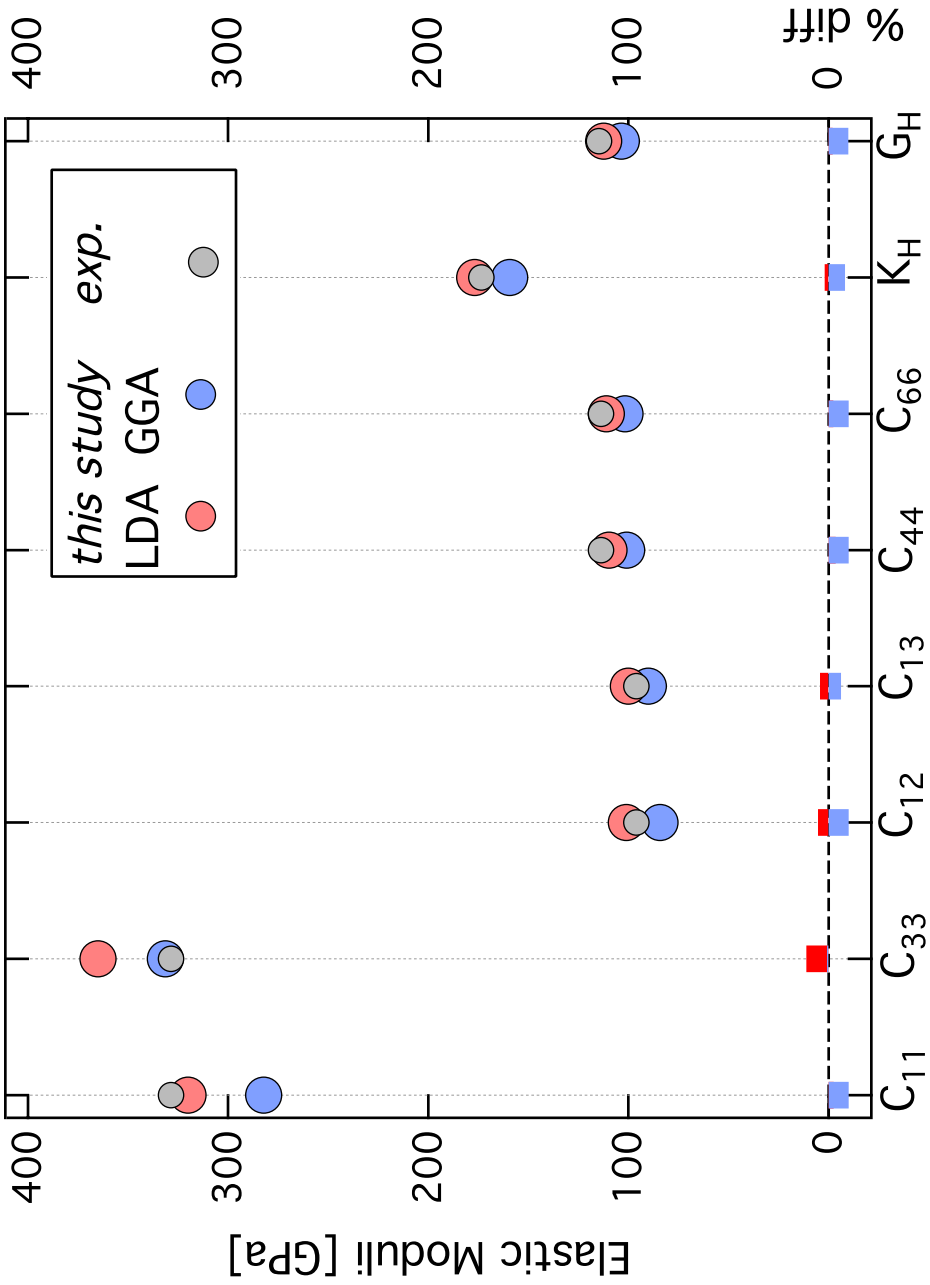
Elastic Moduli [GPa]
% diff
0
100
200
300
400
this study exp.
LDA GGA
C11
C33
C12
C13
C44
C66
KH
GH

Figure 2

This is a preprint, the final version is subject to change, of the American Mineralogist (MSA)
Cite as Authors (Year) Title. American Mineralogist, in press.
(DOI will not work until issue is live.) DOI: http://dx.doi.org/10.2138/am-2014-4956

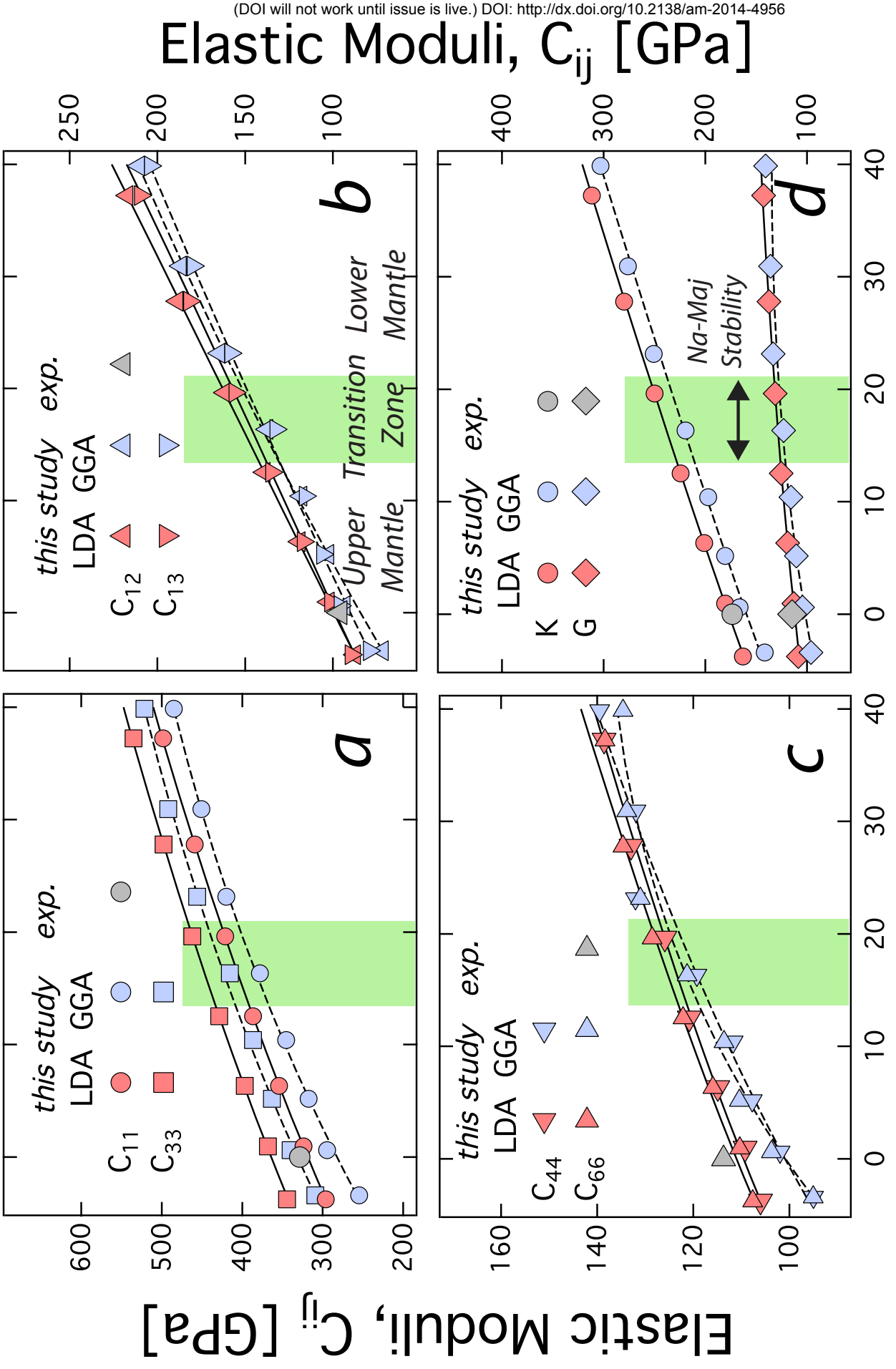

Figure 3

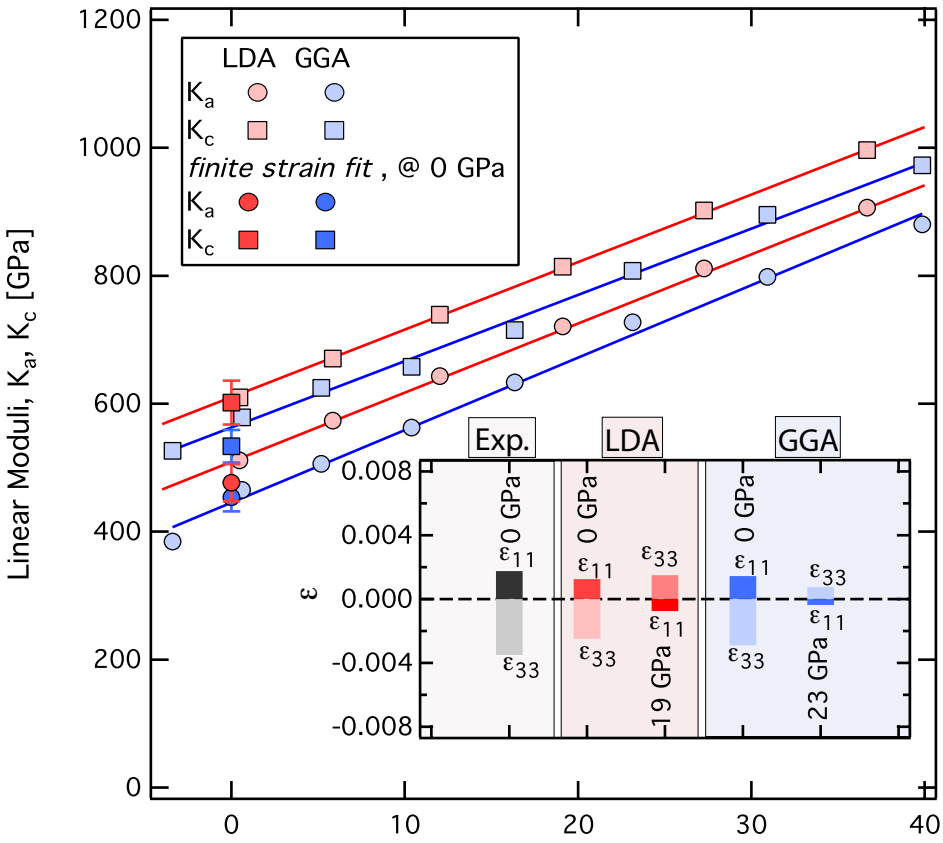
LDA GGA
K_a
K_c
finite strain fit , @ 0 GPa
K_a
K_c
Linear Moduli, K_a, K_c [GPa]
Pressure [GPa]
Exp.
LDA
GGA
ε
0.008
0.004
0.000
-0.004
-0.008
0 GPa
ε_{11}
ε_{33}
19 GPa
23 GPa

Figure 4

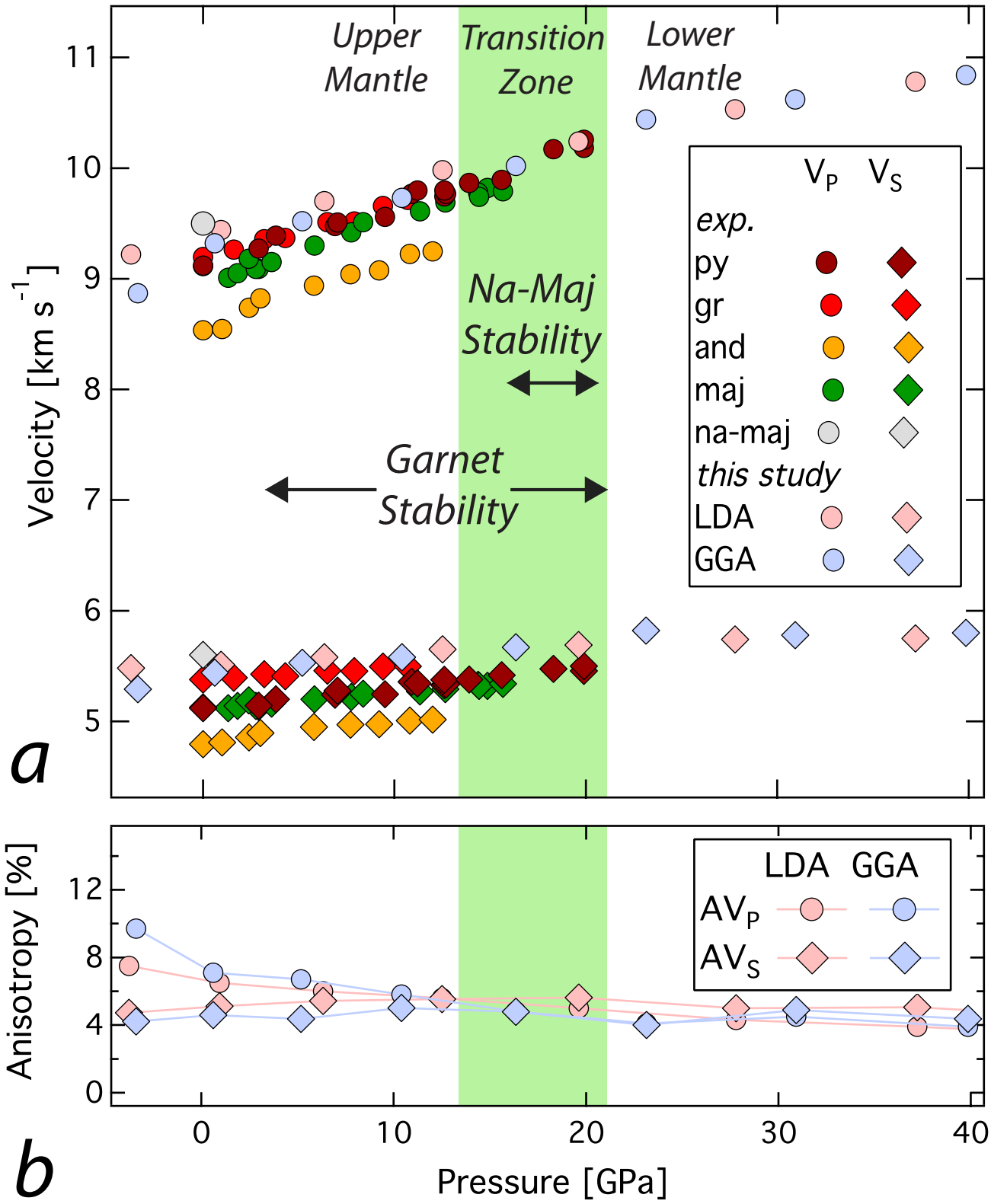
Upper Mantle
Transition Zone
Lower Mantle
Na-Maj Stability
Garnet Stability
Velocity [km s-1]
11
10
9
8
7
6
5
V_P V_S
exp.
py
gr
and
maj
na-maj
this study
LDA
GGA
a
Anisotropy [%]
12
8
4
0
LDA GGA
AV_P
AV_S
b
0
10
20
30
40
Pressure [GPa]

Figure 5